Experiments on Stability of Equilibria of Two Vortices in a Cylindrical Trap

T. B. Mitchell, C. F. Driscoll, and K. S. Fine
Department of Phyiscs and Institute for Pure and Applied Physical Sciences, University of California at San Diego, La Jolla, California 92093

(Received 22 February 1993)

We observe the (r,θ) drift motion of two nearly identical magnetized electron columns bounded by a cylindrical wall. In the 2D $\mathbf{E}\times\mathbf{B}$ drift approximation, these columns are vortices evolving according to the Euler equation. We observe stable and unstable equilibria in which the vortices orbit about the center of the cylinder. The equilibrium positions, oscillation frequencies, and instability rates for these spatially extended vortices agree well with the predictions of integrable point vortex theory, apparently because surface waves and shape distortions do not couple to the center-of-mass motion.

PACS numbers: 47.15.Ki, 52.25.Wz

The dynamics of two-dimensional vortices has been studied for over 100 years, due to the central role of vorticity in fluid dynamics and turbulence. Experiments and simulations have established that vortices can emerge from both laminar flows [1] and structureless initial conditions [2]. The subsequent evolution of these systems can be dominated by the dynamics of the vortices, which includes merger of like-signed vortices and mutual advection. A common assumption has been that the advection can be well described by treating the spatially extended vortices as Hamiltonian point vortices unless they are close enough to merge [3]. However, experimental studies of vortices in water [4], in electrolyte [5], and in superfluid helium [6] have typically found interactions quite different from that predicted for point vortices, apparently because of viscous or boundary effects.

In this Letter, we describe experiments on the stability of two-vortex equilibria, and find quantitative agreement with point vortex theory. The vortices are electron columns with almost identical bell-shaped vorticity profiles, inside a cylindrical Malmberg-Penning trap [7-9]. The equations or (r,θ) motion for the columns are isomorphic to the 2D Euler equations governing the evolution of patches of vorticity in an inviscid fluid of uniform density [10]. Correspondence with 2D theory is particularly close because the electron vortices are reproducibly created and accurately measured, show little dissipation even on time scales of 10^4 orbits, and have no boundary layers at the wall to complicate the dynamics [7].

We observe equilibrium orbits in which two vortices orbit around the center of the cylinder at constant radius. Some of these equilibria are linearly stable, others are unstable. We have measured both oscillations about stable equilibria and exponential divergence from unstable equilibria. The measured equilibrium positions, oscillation frequencies, and instability rates are well predicted by treating the spatially extended vortices as if they were point vortices. The symmetric equilibria of two point vortices within a cylindrical boundary were first analyzed by Havelock [11]; we have recently extended this analysis to consider asymmetric equilibria [9]. Point vortex theory and the experiments both find that the equilibrium orbits are unstable when the orbit radius is more than 0.46 times the wall radius. Moreover, the observed global orbital motions are well predicted from conservation of point vortex energy and angular momentum. Departures from the predictions of the point vortex model occur when the separation between vortices is less than 1.6 times their diameter and merger is observed to occur [8,12], and when the vortices "scrape" the cylindrical wall and circulation (charge) is lost. Also, the axial confinement fields cause a dynamically unimportant shift in the orbit frequencies compared to point vortex theory [13], as will be discussed.

The electron columns are contained in a series of grounded conducting cylinders of radius $R_w = 3.81$ cm, as shown in Fig. 1. The hot tungsten source gives typical electron densities $\tilde{n}(R,\theta,z,t) \lesssim 6\times10^6$ cm^{-3}. A uniform axial magnetic field $B_z = 375$ G provides radial confinement, and negative containment voltages $V_c = -10$ V applied to end cylinders confine the electrons to a length $L_v \approx 20$ cm. We create a two-vortex initial condition by drifting the trapped column a distance D_1 off center, cutting it in half axially with a negative voltage on cylinder B, drifting one column to a new radial distance D_2, adjusting the relative phase of the two columns, and then reexpanding the two columns axially. At any time t during the two-vortex evolution, we obtain the z-averaged electron density $n(R,\theta,t)$ by grounding cylinder C, and

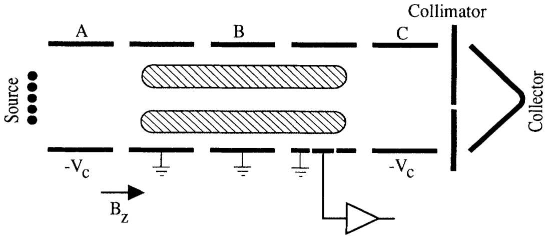

FIG. 1. Schematic diagram of the cylindrical containment system.

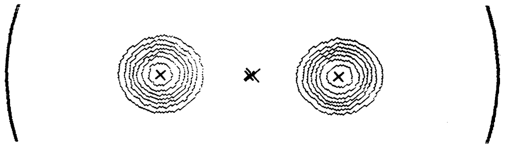

FIG. 2. Measured contour plots of $\hat{\mathbf{z}}$-integrated vorticity (or density) showing two vortices near the stable equilibrium orbit $r_1 = r_2 = 0.36$. The small ×'s mark the centers of mass of the individual vortices and of both vortices together. The large × is the axis of the cylindrical conducting wall, and the arcs indicate the wall radius.

measuring the charge $Q(R,\theta,t)$ which exits through a collimator hole of area $A_h = \pi(1.6\ \text{mm})^2$ centered at (R,θ).

The electron density gives rise to a (z-averaged) potential $\phi(r,\theta,t)$ through Poisson's equation, $\nabla^2\phi = 4\pi e n$, where $-e$ is the electron charge. This results in cross-field drifts, with a flow velocity given by

$$\mathbf{v}(r,\theta,t) = -c\nabla\phi \times \hat{\mathbf{z}}/B_z\,. \tag{1}$$

Mutual advection in this flow field results in the two vortices orbiting around the cylinder axis, with typical frequencies $f_{\text{orb}} \approx 10$ kHz. Additionally, each vortex rotates about its center of mass, at a frequency $f_{\text{rot}} \approx 100$ kHz. The vorticity $\zeta(r,\theta,t)$ of this flow is proportional to the electron density $n(r,\theta,t)$, i.e.,

$$\zeta \equiv \nabla \times \mathbf{v} = \frac{c}{B}\nabla^2\phi = \frac{4\pi e c}{B} n\,. \tag{2}$$

The flow of Eq. (1) is incompressible, and the density (or vorticity) is merely advected in this flow.

Figure 2 is a contour map of density for typical columns, showing bell-shaped profiles extending over a radius $R_v \approx 0.5$ cm, with central density $n(R=0) \approx 3\times10^6$ cm^{-3}. The center of mass for each vortex is marked by a small ×; the cylinder axis is marked by a large ×. For convenience, we hereafter normalize radial coordinates by R_w, e.g., $r_v \equiv R_v/R_w = 0.13$. We characterize the positions of the two identical, spatially extended vortices by the coordinates $(r_1,\theta_1),(r_2,\theta_2)$ of the two centers of mass.

We observe equilibria in which the two vortices orbit about the center of the cylinder, with either $r_1 = r_2$ or $r_1 \neq r_2$, but always with $\theta_2 = \theta_1 + \pi$. In equilibrium, each vortex orbits at a constant radius and with the same frequency f_{orb}, so the two vortices remain diametrically opposed. For $r_1 = r_2$, both stable and unstable equilibria are observed. That is, if the vortices are initially displaced from the equilibrium positions, they either oscillate around the equilibrium points with frequency f_{osc} or diverge from the equilibrium points with an exponential rate γ.

In Fig. 3, the measured orbit radii of the stable equilibria are plotted as circles, and the orbit radii of the unstable equilibria as diamonds. No equilibria are observed for $r_1 = r_2 < 0.22$, since the vortices merge together [8] for $(r_1+r_2)/2r_v \lesssim 1.6$. For larger separations, the $r_1 = r_2$ equilibria are observed to be stable for radii $r < 0.46$ and unstable for $r \gtrsim 0.46$. All $r_1 \neq r_2$ equilibria are observed to be stable; in Fig. 3, these equilibria are shown as circles, with the arbitrary convention of $r_1 > r_2$.

In Fig. 4, we plot the observed rates of oscillation about stable equilibria, f_{osc}, and the observed exponentiation rate from unstable equilibria, γ. These rates, measured in the rotating frame of the orbit, are normalized by the theoretical orbit frequency $f_{\text{orb}}^{\text{th}}$, defined below. For $r_1 = r_2$, f_{osc} varies from approximately $f_{\text{orb}}^{\text{th}}$ down to zero

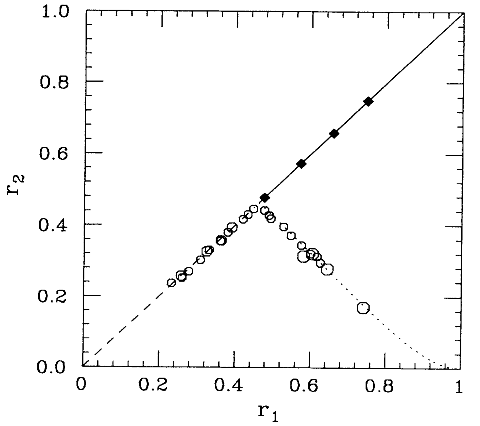

FIG. 3. Measured radial positions of stable (○) and unstable (◆) equilibrium points, where $\theta_2 = \theta_1 + \pi$ for all points. The size of the symbol indicates the estimated uncertainty. The predictions of the point vortex model are also plotted for stable (dashes, dots) and unstable (solid line) points.

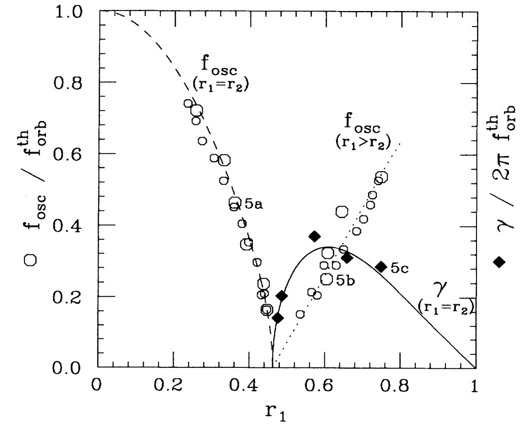

FIG. 4. Normalized measured oscillation frequencies f_{osc} (○) and exponential growth rates γ (◆). The curves show predictions from an analytic point vortex model, where the solid line indicates exponential growth and the dashed and dotted lines are oscillation frequencies. The motions corresponding to the three marked rates are shown in Figs. 5(a)–5(c).

as r_1 is increased from 0.23 to 0.46. For small r, f_{osc} is approximately $f_{\mathrm{orb}}^{\mathrm{th}}$ because the vortices orbit about the center of (total) mass, independent of where this center is relative to the cylindrical wall. As r approaches 0.46, f_{osc} approaches zero, since the restoring forces go to zero as the influence of the image charges in the wall becomes important. For $r_1 = r_2 > 0.46$, initial displacements $\Delta\mathbf{x} \equiv (\Delta r, r\Delta\theta)$ from an equilibrium point are observed to grow exponentially as

$$\Delta\mathbf{x} = A\mathbf{x}_{+}\exp(\gamma t) + B\mathbf{x}_{-}\exp(-\gamma t)\,,$$

where $\mathbf{x}_{+}$ ($\mathbf{x}_{-}$) is the growing (decaying) eigenvector. Over the accessible range of unstable equilibria, we observe growth rates $\gamma/2\pi f_{\mathrm{orb}}^{\mathrm{th}} \approx 0.2$ to 0.4, as shown by the diamonds in Fig. 4.

The observed motion of these spatially extended vortices is well described by a point vortex approximation. This approximation neglects the effects of surface waves and shape distortions, since the fields outside an extended vortex are the same as the fields outside a point vortex only if the extended vortex is circular. In this approximation, we first consider our 3D confined columns as 2D extended vortices of z-averaged density $n(r,\theta,t)$. We then characterize these extended vortices by their area-integrated line density, $N_L \equiv R_w^2 \int 2\pi r\, dr\; n \approx 2\times10^6\ \mathrm{cm}^{-1}$, and treat the two extended patches as two point vortices of circulation $\Gamma \equiv (2\pi c e/B_z) 2N_L \approx 1\times10^6\ \mathrm{cm}^2\,\mathrm{sec}^{-1}$ at the centers of mass.

A point vortex generates an azimuthal velocity field with a magnitude inversely proportional to the distance D from the vortex: $|v| = \Gamma/2\pi D$ [14]. For an equilibrium characterized by $(r_1, r_2, \theta_2 = \theta_1 + \pi)$, therefore, point vortex 1 is predicted to orbit about the cylinder axis at a frequency

$$f_{\mathrm{orb}}^{\mathrm{th}}(r_1,r_2) = \frac{\Gamma}{2\pi}\frac{1}{2\pi r_1}\frac{1}{R_w^2} \times \left[\frac{1}{r_1+r_2} - \frac{1}{r_1+1/r_2} + \frac{1}{r_1-1/r_1}\right]. \quad (3)$$

The three terms in brackets are the inverse distances from vortex 1 to vortex 2, image 2, and image 1, respectively. The orbit frequency of point vortex 2 is given by interchanging the subscripts 1 and 2, so the equilibrium positions are given by the solutions to $f_{\mathrm{orb}}^{\mathrm{th}}(r_1,r_2) = f_{\mathrm{orb}}^{\mathrm{th}}(r_2,r_1)$. In addition to the symmetric solution with $r_1 = r_2$, asymmetric solutions exist with $r_1 > 0.4623 > r_2$, as shown in Fig. 3.

The stability of circular orbits of two or more point vortices within a circular boundary was first analyzed by Havelock [11] in 1931. This linear stability analysis predicts oscillation frequencies f_{osc} around stable equilibria with $r_1 = r_2 < r_H \equiv 0.4623$ and predicts exponentiation rates $\pm\gamma$ for unstable equilibria with $r_1 = r_2 > r_H$, as shown by the dashed and solid curves in Fig. 4. We have extended the linear stability analysis to equilbiria with $r_1 \neq r_2$ [9], and find oscillation frequencies f_{osc} as shown by the dotted curve in Fig. 4. Experimentally, both the stable and unstable dynamics of the 3D electron columns are well described by the 2D point vortex approximation.

Interestingly, the full nonlinear motion of two point vortices within a cylindrical boundary can be understood from phase space maps, since the system is integrable. There are four variables and two constants of the motion, the angular momentum per unit length $\mathcal{P}_\theta$, and the interaction energy per unit length $\mathcal{H}$ [14,15]. These are written in scaled variables P_θ and H as

$$P_\theta = \frac{\mathcal{P}_\theta}{\mathcal{P}_0} = \sum_{i=1,2}(1-r_i^2) \quad (4)$$

and

$$H = \frac{\mathcal{H}}{\mathcal{H}_0} = \sum_{i=1,2}\ln(1-r_i^2) + \ln\left[1 + \frac{(1-r_1^2)(1-r_2^2)}{r_{12}^2}\right]. \quad (5)$$

Here, $\mathcal{P}_0 \equiv (eB/2c)R_w^2 N_L$ is the angular momentum of an on-axis line charge, and we choose $P_\theta = 0$ at $r = r_w = 1$. $\mathcal{H}_0 \equiv e^2 N_L^2$ is a characteristic energy, and $r_{12}^2 = |\mathbf{r}_1 - \mathbf{r}_2|^2 = r_1^2 + r_2^2 - 2r_1 r_2\cos(\theta_1 - \theta_2)$.

The motion of the point vortices can be visualized from contour maps of $H(r_1, \theta_1 - \theta_2, P_\theta)$. For any given P_θ, the vortices move along a contour of constant H. Given r_1, the second vortex must be at $r_2^2 = 2 - r_1^2 - P_\theta$. There are three distinct map topologies over the accessible range of $0 < P_\theta < 2$, and examples of these are shown in Fig. 5. For $P_\theta > 2(1 - r_H^2)$, there is a minimum energy stable equilibrium (an ○ point) with the two vortices symmetrically opposite each other, i.e., $\theta_1 - \theta_2 = \pi$ and $r_1 = r_2$, as shown in Fig. 5(a). For $1 < P_\theta < 2(1 - r_H^2)$, the symmetric equilibrium is an unstable saddle point (an × point), and two new ○ points exist at $r_1 \neq r_2$ values [Fig. 5(b)]. As P_θ decreases, the ○ points move further from the × point, until for $P_\theta < 1.0$ there are no stable equilibra [Fig. 5(c)].

Also shown by the □ and + symbols in Fig. 5 are the measured center-of-mass coordinates of the two vortices, for evolutions with the corresponding P_θ. In Fig. 5(a), the center of mass of each vortex is observed to oscillate once around the stable equilibrium while the vortices orbit 2.7 times around the cylindrical center. The uncertainty in the measured positions corresponds to an uncertainty in energy of $\delta H \lesssim 0.01$. In Fig. 5(b), $\frac{3}{4}$ of an oscillation about an asymmetric equilibrium is observed, with a larger measurement error corresponding to $\delta H \approx 0.02$ due to additional uncertainties introduced while creating the $r_1 \neq r_2$ equilibria. In Fig. 5(c), the vortices exponentiate away from the unstable equilibrium, with the displacements being largely in the θ direction. The large measurement errors at long times reflect the difficulty in repeatedly following the exponentially unstable trajectories.

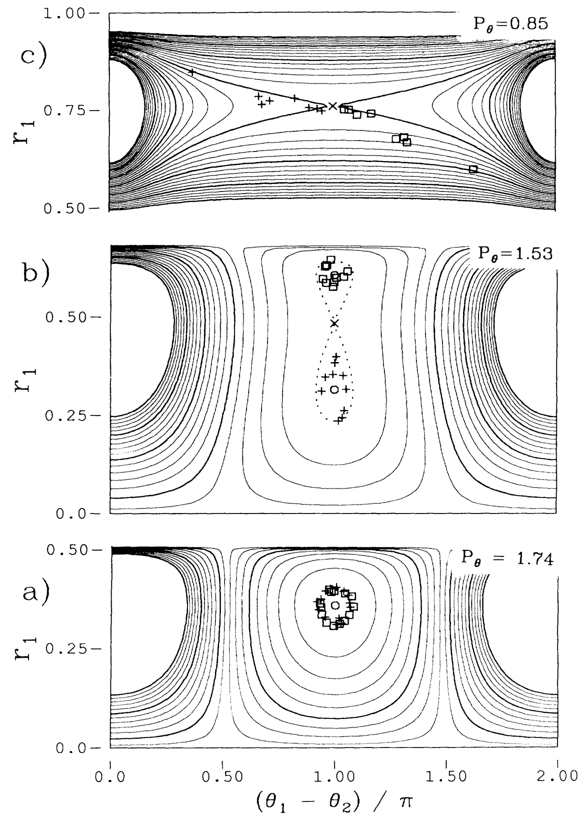

FIG. 5. Energy contours in configuration space for three values of scaled angular momentum P_θ. Minima (○) and saddle points (×) are shown, as are the measured center-of-mass positions of two vortices (□ and +) at a sequence of times. The energy difference between contours is $\Delta H = 0.05$. (a) $P_\theta = 1.74$. One energy minima is at $r_1 = r_2$. (b) $P_\theta = 1.53$. $r_1 = r_2$ is a saddle point, and two energy minima exist with $r_1 \neq r_2$. An additional energy contour (dots) at the value of the saddle point is included. (c) $P_\theta = 0.85$. No stable energy minima are seen.

For spatially extended vortices, the energy H will include self-energy and interaction energy terms which depend on the shapes of the vortices. Experimentally, we observe elongations away from circularity of $\lesssim 10\%$ in general, and up to 30% for $r_1 = r_2 \sim 0.23$ (near merger). These time-varying eccentricities have not, however, been observed to casue experimentally noticeable departures from the predictions of the point vortex model. This result is perhaps because the energies involved in elongation are relatively small: Using a moment model [12], we estimate $\delta H \sim 0.002$ and 0.02 for elongations of 10% and 30%, respectively.

The main discrepancy between the observed motions and the predicted 2D point vortex dynamics is that the observed orbit frequencies f_{orb} are uniformly about 2.1 kHz greater than the predicted $f_{\text{orb}}^{\text{th}}$. This frequency shift is a 3D (finite length) effect, due to the confinement forces required at the ends of the columns; it is also seen in the orbit of a single off-center vortex, i.e., the $l = 1$ diocotron mode [8,13]. This shift in f_{orb} is observed to be nearly independent of the orbit radius [9]. Therefore, the net effect is just a shift of rotational frame, leaving the vortex dynamics unchanged with f_{osc} and γ as predicted by 2D theory.

In conclusion, we find that the point vortex model accurately predicts the motions of extended vortices as long as the vortices are not susceptible to merger, or in contact with the wall. Thus, we find that the overall stability of this obviously nonintegrable system is well described by the integrable point vortex approximation. This is apparently because the internal degrees of freedom associated with (r, θ) shape distortions do not significantly couple to the center-of-mass motion.

We wish to acknowledge enlightening discussions with Ralph A. Smith and John H. Malmberg. This work was supported by the Office of Naval Research Grant No. N00014-89-J-1714, Department of Energy Grant No. DE-FG03-85ER53199, and National Science Foundation Grant No. PHY91-20240.

[1] P. Freymuth, J. Fluid Mech. **25**, 683 (1966).
[2] J. C. McWilliams, J. Fluid Mech. **146**, 21 (1984).
[3] R. Benzi, S. Patarnello, and P. Santangelo, Europhys. Lett. **3**, 811 (1987).
[4] R. W. Griffiths and E. J. Hopfinger, J. Fluid Mech. **178**, 73 (1987).
[5] P. Tabeling *et al.*, Phys. Rev. Lett. **67**, 3772 (1991).
[6] E. J. Yarmchuk and R. E. Packard, J. Low Temp. Phys. **46**, 479 (1982).
[7] C. F. Driscoll and K. S. Fine, Phys. Fluids B **2**, 1359 (1990).
[8] K. S. Fine, C. F. Driscoll, J. H. Malmberg, and T. B. Mitchell, Phys. Rev. Lett. **67**, 588 (1991).
[9] T. B. Mitchell, Ph.D. dissertation, University of California, San Diego, 1993.
[10] R. H. Levy, Phys. Fluids **8**, 1288 (1965).
[11] T. H. Havelock, Philos. Mag. S.7. **11**, 617 (1931).
[12] M. V. Melander, N. J. Zabusky, and J. C. McWilliams, J. Fluid Mech. **195**, 303 (1988).
[13] K. S. Fine, Bull. Am. Phys. Soc. **36**, 2331 (1991).
[14] H. Aref, *Theoretical and Applied Mechanics* (International Union of Theoretical and Applied Mechanics, Amsterdam, 1985).
[15] T. M. O'Neil, Phys. Fluids **23**, 2216 (1980).